

# Deployment and validation of predictive 6-dimensional beam diagnostics through generative reconstruction with standard accelerator elements

Seongyeol Kim,<sup>1,\*</sup> Juan Pablo Gonzalez-Aguilera,<sup>2</sup> Ryan Roussel,<sup>3,†</sup> Gyujin Kim,<sup>1</sup> Auralee Edelen,<sup>3</sup> Myung-Hoon Cho,<sup>1</sup> Young-Kee Kim,<sup>2</sup> Chi Hyun Shim,<sup>1</sup> Hoon Heo,<sup>1</sup> and Haeryong Yang<sup>1,‡</sup>

<sup>1</sup>*Pohang Accelerator Laboratory, POSTECH, Pohang, Gyeongsangbuk-do 37673, Republic of Korea*

<sup>2</sup>*Department of Physics and Enrico Fermi Institute, University of Chicago, Chicago, IL 60637, USA*

<sup>3</sup>*SLAC National Accelerator Laboratory, Menlo Park, CA 94025, USA*

Understanding the 6-dimensional phase space distribution of particle beams is essential for optimizing accelerator performance. Conventional diagnostics such as use of transverse deflecting cavities offer detailed characterization but require dedicated hardware and space. Generative phase space reconstruction (GPSR) methods have shown promise in beam diagnostics, yet prior implementations still rely on such components. Here we present the first experimental implementation and validation of the GPSR methodology, realized by the use of standard accelerator elements including accelerating cavities and dipole magnets, to achieve complete 6-dimensional phase space reconstruction. Through simulations and experiments at the Pohang Accelerator Laboratory X-ray Free Electron Laser facility, we successfully reconstruct complex, nonlinear beam structures. Furthermore, we validate the methodology by predicting independent downstream measurements excluded from training, revealing near-unique reconstruction closely resembling ground truth. This advancement establishes a pathway for predictive diagnostics across beamline segments while reducing hardware requirements and expanding applicability to various accelerator facilities.

Particle accelerator-based user facilities are indispensable tools that power scientific discovery in the biological, chemical and material sciences [1, 2]. Understanding the precise distribution of particles in an accelerated beam is therefore critical to improving and maintaining optimal performance of these facilities. For example, X-ray Free Electron Laser (XFEL) facilities are strongly dependent on the distribution of electrons in 6-dimensional position-momentum space to generate high-brightness, ultra-short X-ray pulses [3–11]. The precise structure of the beam distribution during the acceleration and compression stages of the accelerator impacts overall beam quality due to collective effects such as space charge and coherent synchrotron radiation (CSR) [12–17], that in turn, negatively impacts FEL performance. As a result, methods are needed to efficiently and precisely characterize 6-dimensional phase space distribution at multiple locations along the beamline.

While methods for measuring lower dimensional phase space distribution structure of particle beams are well understood, either through sub-sampling portions of the beam distribution [18, 19] or via tomographic manipulations [20–24], their applicability becomes limited on 5- [25, 26] or 6-dimensional [27] phase space distributions due to largely increased number of samples required by the nature of the tomography. Previous attempts at characterizing the high-dimensional phase space distribution of beams require a substantial amount of dedicated experimental beam time to conduct (>18 hrs for 6-dimensional characterization [27]), making these methods impractical for use at user facilities. Additionally,

these methods also require the use of specialized diagnostic elements to characterize the beam distribution, such as movable slits or transverse deflecting cavities (TCAVs) [28–31]. These additional requirements can add complexity and operational costs to diagnose the beam at multiple locations and reduce high-value space in the accelerator beamline.

Recently, machine learning methods have been used to create so-called “virtual diagnostics” that are able to predict the phase space distributions from beamline parameters and/or experimental measurements [32–39]. These predictive models are trained on simulated data, where, for a given set of accelerator parameters, the true beam distribution at the location of the virtual diagnostic is known from beam physics principals. However, these methods rely on training data generated from accurate physics models of entire accelerator beamlines, which can become prohibitively difficult to effectively calibrate to match experimental accelerator conditions at the level of precision needed to resolve precise beam distributions.

More recently, a new machine learning technique, known as generative phase space reconstruction (GPSR), has been developed to address the limitations of high-dimensional characterization and predictive methods [40]. A schematic of the GPSR technique is as follows [see Fig. 1a]: the initial 6-dimensional phase space distribution is parameterized by a transformer-based, generative machine learning model that is able to flexibly generate a wide variety of distribution structures. The initially generated beam is then propagated through a simulated version of the beamline using a differentiable particle tracking software [41]. To reconstruct the beam distribution, the parameters of the generative model are iteratively updated via gradient descent optimization [42] to minimize the difference between experimental measurements of the  $(x, y)$  beam distribution on intercepting

\* [sykim12@postech.ac.kr](mailto:sykim12@postech.ac.kr)

† [rroussel@slac.stanford.edu](mailto:rroussel@slac.stanford.edu)

‡ [highlong@postech.ac.kr](mailto:highlong@postech.ac.kr)

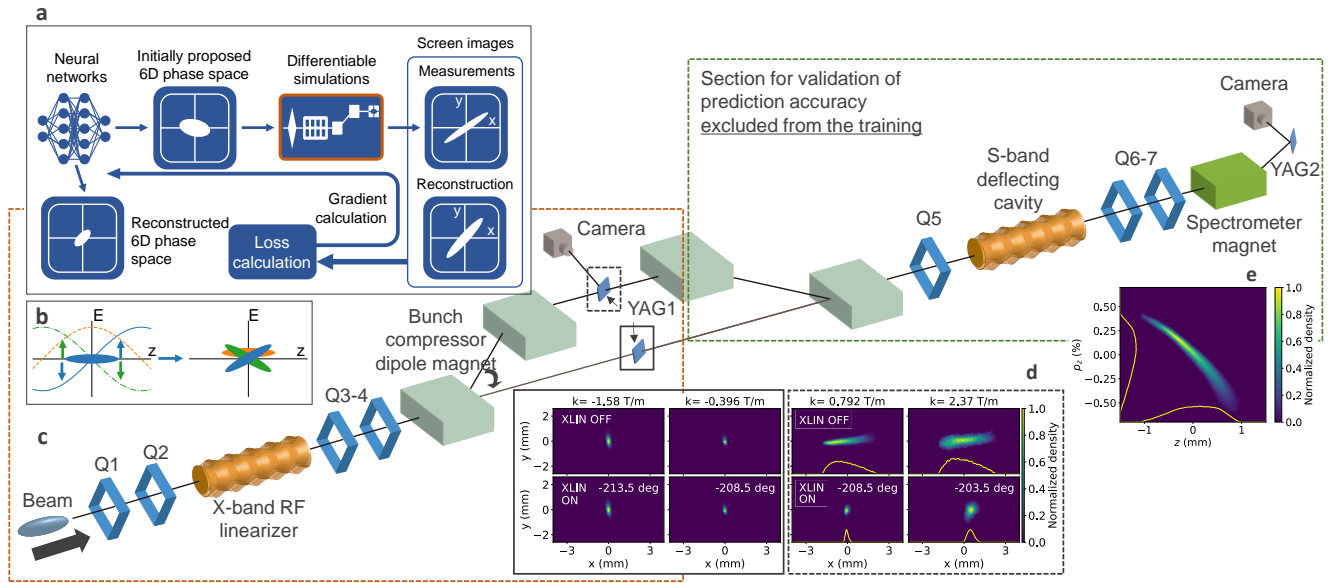


FIG. 1. **a.** Schematics of the GPSR method [40]. **b:** Cartoon showing an evolution of beam energy chirp by the accelerating field. **c:** Schematic view of the first bunch compressor section at the PAL-XFEL, where the longitudinal phase space is measured at YAG2 screen using S-band TCAV and spectrometer [e. measured longitudinal phase space for BC and XLIN OFF]. Nominal beam charge and measured kinetic energy are 250 pC and 260.5 MeV, respectively. The lattice used for the reconstruction training process is in the dashed orange box. **d.** Beam images at the YAG1 screen with various BC, XLIN, and Q1 conditions.

screens and corresponding simulated predictions. Minimizing the difference ultimately yields the reconstructed beam phase space distribution that reproduces experimental measurements.

Previous experimental demonstrations of the GPSR method [40, 43, 44] have shown a dramatic reduction in the number of experimental measurements needed to reconstruct 4 to 6-dimensional phase space distributions, leading to the corresponding reduction in the amount of beam time required to perform those measurements. Nonetheless, its broader applications at the accelerator facilities remains limited, as it still relies on specialized diagnostic elements such as TCAVs to rotate and probe the beam distribution in 6-dimensional phase space. In addition, prior studies have primarily focused on validating reconstructions at a specific diagnostic point, leaving predictive accuracy and uncertainty quantification at additional downstream locations unexplored.

In this work, we demonstrate the first implementation and validation of the GPSR methodology for complete 6-dimensional phase space reconstruction using standard beamline elements commonly available at accelerator facilities [2, 45, 46], including accelerating cavities and spectrometer magnets. Through both simulation and experiment at the user facility, Pohang Accelerator Laboratory X-ray Free Electron Laser (PAL-XFEL) [10, 11, 47], we show that a combination of quadrupole scans, dispersive measurements, and the accelerating cavity phase scans provides sufficient information to reconstruct the detailed 6-dimensional phase space distribution of the beam including complex and nonlinear features. Fur-

thermore, we conduct the first experimental validation of the reconstruction methodology by accurately predicting independent, downstream experimental measurements of the beam phase space, such as a longitudinal phase space (LPS) and transverse-energy correlations at the end of the beamline (located approximately 27 m from the reconstruction region) excluded from the training process. These downstream observations insofar are the best evidence of GPSR predictive accuracy, revealing that the reconstructed phase space closely approximates the ground truth physical distribution. This work shows that the reconstruction framework enables efficient, high-fidelity 6-dimensional phase space diagnostics using only standard elements, and establishes a foundation for predictive, uncertainty-aware diagnostics in a wide range of accelerator facilities.

## I. RESULTS

### A. GPSR methodology with standard beamline elements

Previous 6-dimensional phase space reconstructions relied on the spectrometer magnets and TCAVs to directly measure the longitudinal correlations. In contrast, we show in this demonstration that these correlations can be extracted using only the spectrometer and accelerating cavity readily available in most accelerator facilities. Here, we should note that the methodology is not limited to this particular setup, but can be adapted to other stan-

dard beamline configurations that establish phase space correlations.

The key insight of the methodology can be conceptualized as a decomposition of the full reconstruction process into several components, each informed by physical measurements along the beamline. First, the 4-dimensional transverse phase space  $(x, x', y, y')_i$  is reconstructed using quadrupole scans and transverse beam distributions measured at a screen along the straight beamline [40] as shown in Fig. 1c. Here, we note that 6-dimensional phase space of the beam is described by  $(x, x', y, y', z, \delta)$  with  $x' = p_x/p_z$ ,  $y' = p_y/p_z$  where  $p_{x,y,z}$  indicates momentum in  $(x, y, z)$  plane, and  $\delta = (p_z - p_{z,ref})/p_{z,ref}$ , respectively. Subscripts  $i$  and  $f$  denote the initial and final states. The reconstructed transverse phase space is then treated as known input for dispersive measurements. Accordingly, the horizontal beam distribution  $x_f$  observed at the same screen with the spectrometer activated allows inference of the fractional energy spread  $\delta_i$  through the dispersive measurement, as described in Eq. (1).

$$x_f = R_{11}x_i + R_{12}x'_i + R_{16}\delta_i, \quad (1)$$

where  $R_{11}$ ,  $R_{12}$  are transfer matrix components and  $R_{16}$  is a dispersion, which are all determined by the beamline optics. Therefore, through the GPSR process with measurements in straight line and dispersive section, 5-dimensional phase space  $(x, x', y, y', \delta)_i$  becomes resolved.

To recover the longitudinal coordinate  $z_i$ , we utilized the energy modulation generated by the accelerating cavity. As the beam propagates through the cavity, its energy evolves as

$$E_f = E_i + eV \sin(k_{RF}z_i + \phi_{RF}), \quad (2)$$

where  $k_{RF}$  and  $\phi_{RF}$  are wavenumber and phase of the accelerating cavity, respectively.  $E_i$  and  $E_f$  are initial and final energy distributions. By activating or deactivating the accelerating cavity, we can clearly obtain the change of the beam energy  $\Delta E$  that is related to the fractional energy spread  $\delta_i$ . This enables reconstruction of the 1-dimensional projected  $z_i$  distribution associated with  $\delta_i$ .

To further resolve the correlation between  $z_i$  and  $\delta_i$  including longitudinal phase space information, we perform RF phase scans. These phase scans modulate the energy gain along the beam as depicted in Fig. 1b [48, 49], leading to the longitudinal phase space rotation that allows the extraction of second-order moments [50]. This procedure is conceptually analogous to quadrupole scans in the transverse plane, where beam envelope evolution is used to calculate the transverse emittance. Finally, by incorporating the quadrupole and cavity phase scans into the GPSR training process, we can achieve full 6-dimensional phase space reconstruction using only standard beamline elements.

In particular, since the 5-dimensional phase space is explicitly determined by measurements, the reconstruc-

tion of the longitudinal coordinate  $z_i$  is strongly constrained by the intrinsic  $(z, \delta)$  correlations described in Eq. (2). Thus, this reconstruction process enables recovery of additional correlations associated with  $z_i$ , yielding a nearly unique solution that closely approximates the 6-dimensional phase space of the beam. Thus, it has direct implications regarding prediction accuracy and uncertainty quantification. We will investigate these factors with independent downstream measurements in the following sections.

## B. Experimental setup

A schematic of the beamline elements used in the demonstration is shown in Fig. 1c. We used an X-band RF accelerating cavity (XLIN) to obtain controlled energy modulations [51], which is typically used to linearize the non-linear energy chirp [52] in XFEL facilities. For the transverse phase space rotation, we used Q1 quadrupole magnet. We used the first two dipole magnets in the bunch compressor (BC) section as the spectrometer. Particularly, the BC is mounted on the movable stage support, allowing it to be configured into a straight line [53]. In this configuration, we can measure the projected  $(x, y)$  beam distributions at the straight and dispersive sections with the YAG1 screen as shown in Fig. 1c-d (See Methods for more details on the experimental setup).

Downstream of the GPSR section comprises 3 quadrupole magnets, S-band TCAV, spectrometer magnet, and the YAG2 screen. This section is mainly used to measure the longitudinal phase space and other position-momentum correlations to investigate the prediction accuracy with independent downstream measurements. It should be highlighted that that all downstream measurements are not included in the training process and used solely for validation. Total length of the beamline from the Q1 to YAG2 is roughly 27 m.

In the data acquisition, we sampled beam distributions using a combination of 16 Q1 magnet strengths and 8 XLIN phase settings (see Methods for more details of the setup). An additional setting with the XLIN cavity turned off was included to obtain the initial  $(z, \delta)$  correlations of the beam before manipulation by the XLIN cavity. Accordingly, there are a total of 9 XLIN phases. For each beamline configuration, we took 15 shots at a repetition rate of 2 Hz with a charge window within  $\pm 3\%$  of the nominal bunch charge of 250 pC. The measured images were then averaged, and then resulting beam distribution was used as a data sample for the reconstruction process. The total number of data samples was  $16 \times 9 \times 2 = 288$ , where the factor of 2 corresponds to the spectrometer configurations (BC ON/OFF). It was then split in half to create a training dataset (144 samples) which was used to reconstruct the beam distribution, and a test dataset used to validate the accuracy of reconstruction predic-

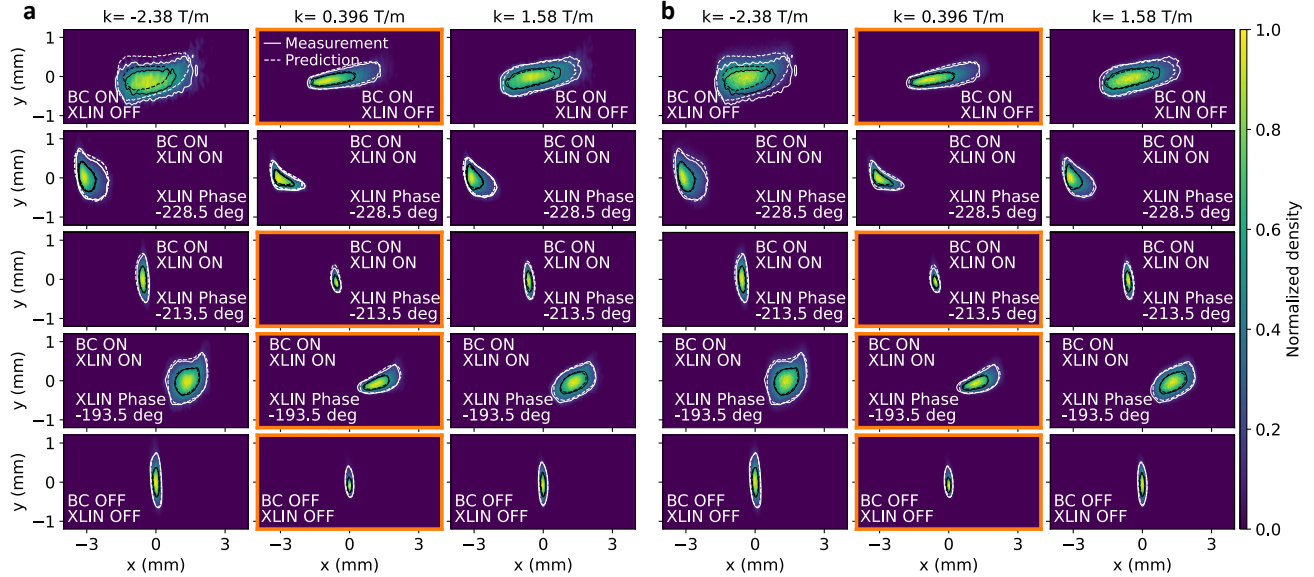


FIG. 2. Comparison between measured beam distributions and predictions at the YAG1 screen. Training dataset is highlighted with orange box. White(black) contour line indicates 90th(50th) percentile, where solid(dashed) lines represent the measurement(prediction). Background image shows the measurement for **a**, while it illustrates the prediction for **b**.

tions.

The training dataset generated during the experiment was then combined with a differentiable model. The differentiable beam dynamics simulation was built using the Bmad-X [41] Python library, which implements up to second order beam tracking through the RF and magnetic elements using backwards differentiable calculations in PyTorch [54]. In this simulation, collective effects such as space charge or coherent synchrotron radiation (CSR) effects were neglected, as simulations using the ELEGANT code [55] indicated that these effects have negligible impact in this region of the beamline.

Initial training was performed using the full set of 144 training samples with 2,400 iterations (See Methods for details of the reconstruction setup). We subsequently confirmed that the comparable GPSR performance can also be achieved using a reduced dataset and training iterations; it took approximately 30 minutes for 1,000 iterations on an NVIDIA A100 GPU at NERSC [56], where we used the dataset from only 5 XLIN phases (80 samples).

### C. Prediction of training and test datasets from the reconstructed phase space

Prior to the experimental demonstration, we conducted a simulation-based validation of the reconstruction methodology using the beamline configuration described above. We evaluated the accuracy on three representative 6-dimensional phase space distributions: i) a coupled Gaussian beam distribution, ii) a nonlinearly structured beam containing a double-horn energy pro-

file, and iii) a realistic beam distribution obtained from upstream beam dynamics simulations of the nominal PAL-XFEL beamline. We found that the reconstruction methodology under the similar parameter scan conditions as in the experiment was able to accurately reconstruct qualitative and quantitative features of the beam. The simulated data analysis are shown in the Supplementary Figs. 4-15. In addition, we emphasize that the prediction of particle samples from a 6-dimensional phase space distribution is produced through the reconstruction process, which can be used to make predictions of beam dynamics or beam properties at different beamline settings or at different locations along the beamline.

First, Fig. 2 shows a comparison between experimental measurements and reconstruction predictions for a subset of training and test settings at the YAG1 screen. In this figure, the background image in **a(b)** represents the measurement(prediction) [see Supplementary Figs. 1-2 for comparisons using the full datasets]. In case of the dispersive measurements with the XLIN turned off (top row), small discrepancies are observed between the predicted and measured distributions, likely due to the low signal-to-noise ratios (SNR) or RF phase drift of accelerating cavities upstream of the demonstration section. However, these small deviations do not compromise the ability of the trained model to capture detailed features of the beam, and they further demonstrate the robustness of the methodology in the presence of measurement noise.

Overall, the reconstructed beam distribution successfully reproduces shape and density of the measured distributions, including nonlinear features such as asymmetric tails. In addition, we observed a clear modulation

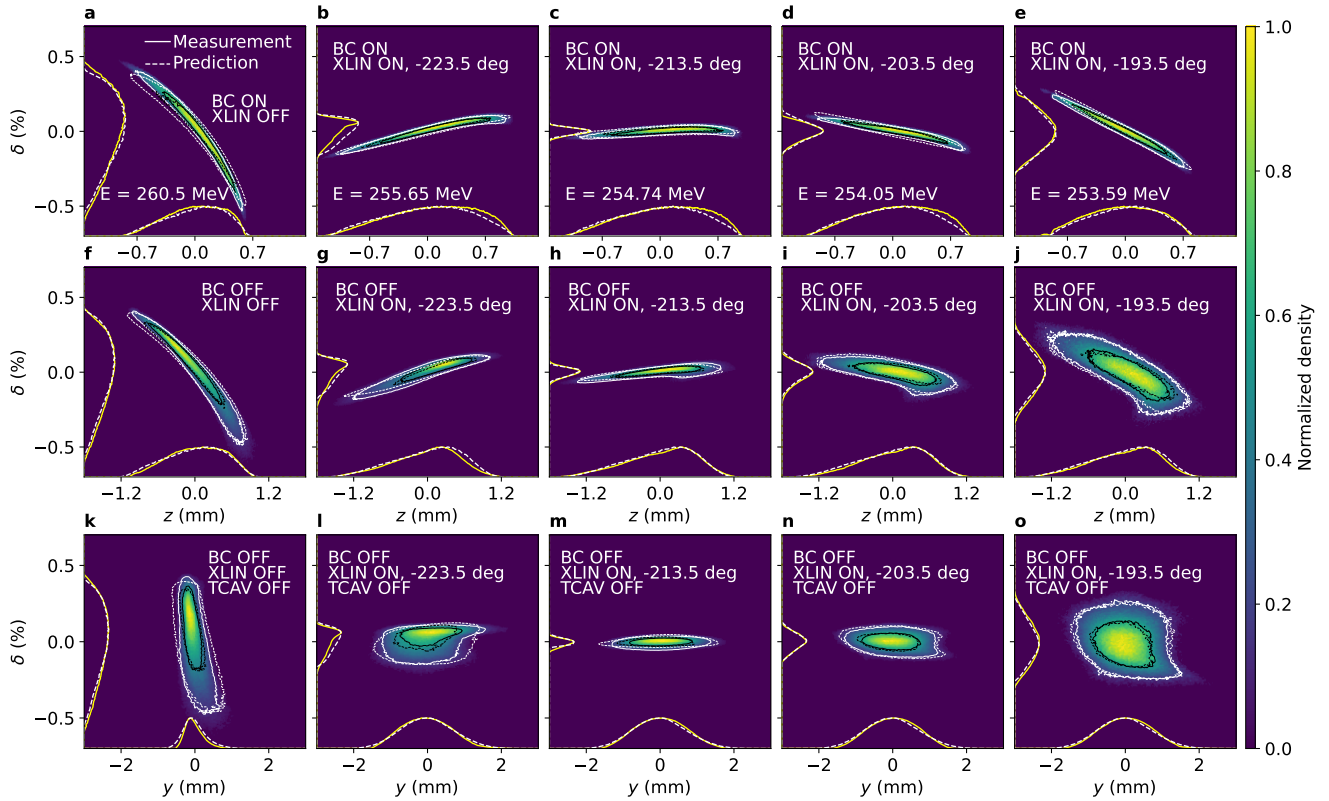


FIG. 3. Comparison of LPSs and  $(y, \delta)$  correlations at the YAG2 screen. In case of the LPS, the beam head is placed at positive  $z$  while the tail is at negative  $z$ . Background image indicates the measured distribution. The average kinetic energy is indicated in each sub-figure, as the  $\delta$  is distributed with respect to zero. White dashed(yellow solid), projected histogram indicates predicted(measured) density distribution. White(black) contour line indicates 90th(50th) percentile. Top row **a-e**: LPS where BC ON. Middle row **f-j**: LPS where BC OFF. Bottom row **k-o**:  $(y, \delta)$  correlations with BC OFF.

of the beam centroid position as the XLIN cavity phase varies. This modulation indicates the energy-dependent change in beam trajectory with the fixed magnetic field of the dipole magnets, which highlights capabilities of the reconstruction methodology to infer the energy changes associated with the longitudinal coordinate  $z_i$  from transverse beam measurements only.

#### D. Validation of the methodology via independent downstream measurements

In addition to analyzing the training and test datasets, a critical component of validating the methodology is the comparison of reconstructed beam characteristics with independent downstream measurements that are completely excluded from the training process. We propagated the reconstructed 6-dimensional distribution through the remainder of the beamline using the ELEGANT simulation code, which takes into account collective and nonlinear optical effects such as coherent synchrotron radiation and chromatic aberrations. The resulting predicted beam distributions were then compared with experimental measurements at the YAG2 screen, lo-

cated 27 m downstream from the reconstruction point. These measurements were obtained using a combination of quadrupole magnets, S-band TCAV, and spectrometer dipole as shown in Fig. 1c.

Figure 3 presents a comparison between simulated predictions and experimental measurements of the longitudinal phase space and  $(y, \delta)$  correlations under a variety of beamline conditions (see Methods for details on YAG2 measurements and Supplementary Fig. 3 for additional comparisons). The image observed at the YAG2 screen represents the projected  $(z, \delta)$  distribution in  $(x, y)$  plane by means of the TCAV and spectrometer magnet. This implies that focusing effects by quadrupole magnets located around the diagnostic region introduce additional transverse correlations on the beam, distorting the projected  $(z, \delta)$  mapping. Thus, the measured image is a result of both longitudinal and transverse phase space projections.

Despite these inherent complexities of downstream measurements, the reconstructed beam distribution accurately predicts the 1-dimensional projected histograms along the longitudinal coordinates  $z$  and  $\delta$ , showing excellent agreement with experimental measurements. In addition, the 2-dimensional phase space densities obtained

from the reconstruction almost match the measured distributions, successfully capturing nonlinear correlations and rotation of the longitudinal phase space. The reconstruction also recovers key features of the beam before the manipulation by the XLIN cavity including bunch length compressions, when the entire bunch compressor section is active (see horizontal axis  $z$  in Fig. 3a-j).

Furthermore, the reconstruction successfully reproduces transverse-longitudinal correlations ( $y, \delta$ ) as shown in Fig. 3k-o [see also Supplementary Figs. 6, 10, and 14, which illustrate other correlations from simulated demonstrations, such as ( $x, \delta$ ) and ( $x', z$ )]. Although slight discrepancies between predicted and measured 1- and 2-dimensional projections are observed in some cases, these are minor relative to the overall beam structure. Whether such deviations originate from the trained model or imperfections in the simulation of the beamline compared to the actual experimental setup remains a subject of future works.

Nevertheless, these results confirm that the reconstruction methodology is able to accurately predict independent downstream measurements, demonstrating not only the robustness of the predictive diagnostics, but also that the initially reconstructed distribution can be considered close approximation to the actual physical beam. Thus, this validation indicates that predictive diagnostics are applicable at any beamline locations along the reconstruction section. In addition, predictive diagnostics can be extended to further downstream positions with the calibrated simulation lattice which is almost identical to the experimental condition.

### E. Reconstructed 6-dimensional beam phase space

Finally, Fig. 4 illustrates the reconstructed 6-dimensional phase space of the beam at the entrance to the Q1 magnet. Figure. 4a shows 2-dimensional projections of the beam distribution, providing a comprehensive view of the correlations among all beam coordinate axes, while Fig. 4b shows a subset of 3-dimensional projections along coordinate axes. The reconstruction predicts non-linear tails in the transverse dimensions and accurately reproduces the nonlinear energy chirp, as observed by direct measurements shown in Fig. 3

We also calculated ensemble-averaged quantities of the beam as summarized in Table I. The 6-dimensional reconstruction accurately reproduces transverse emittance values and Twiss parameters. These predicted values have quantitative agreement within 10% of those obtained by 4-dimensional phase space reconstructions using the GPSR analysis procedure outlined in [40]. For the longitudinal phase space at the end of the beamline, the reconstructed values agrees well with conventional calculations of longitudinal bunch properties, such as the RMS longitudinal bunch length, momentum deviation, and emittance (where uncertainty estimates come from systematic uncertainties in image thresholding, see details in Meth-

ods). Finally, the RMS slice energy spread—a critical quantity of interest for XFELs—is predicted to be 0.01%, which is consistent with typical values observed during normal operations at the PAL-XFEL.

In addition, we investigated the uncertainty by performing multiple reconstruction runs under different configurations of the number of iterations and data samples for the training. This analysis aims to evaluate the robustness and reproducibility of the methodology with respect to random initialization of neural networks and update of the particle distribution via gradient-based optimizations. We considered 3 additional cases: i) training with all 144 datasets for 2,400 iterations, ii) training with the same datasets for 1,200 iterations, and iii) training with 80 datasets using different XLIN phase settings for 1,000 iterations. The reconstructed beam parameters listed in Table I in parentheses indicates the averaged values with standard deviation  $1\sigma$ . It shows that the reconstruction methodology provides well converged values, exhibiting low sensitivity to random seeding variations. Furthermore, we found that the predicted beam distributions for those cases also remain in qualitative agreement with the experimental measurements.

## II. DISCUSSIONS

We have validated prediction accuracy of the GPSR methodology using standard accelerator elements, including the accelerating cavity and spectrometer magnet, without relying on specialized deflecting structures to extract ( $z, \delta$ ) correlations. The reconstructed 6-dimensional phase space not only shows excellent agreement with the training and test datasets, but also remains in quantitatively and qualitatively agreement with measured beam distributions further downstream in the beamline, which are excluded from the reconstruction training. These observations provides strong evidence that the GPSR can be effectively applied to systems that establish transverse-longitudinal correlations, regardless of the specific source, thereby greatly enhancing its flex-

TABLE I. Comparison of the Twiss parameters, emittances, and RMS quantities. Values in parenthesis show the averaged values with standard deviation  $1\sigma$  for several different GPSR setup. See Sec. I E for more details on the setup.

Case	4D reconstruction	6D reconstruction	unit
$\epsilon_{nx}$	0.42	0.40 ( $0.42 \pm 0.01$ )	mm mrad
$\epsilon_{ny}$	0.39	0.40 ( $0.39 \pm 0.01$ )	mm mrad
$\beta_x$	4.53	4.67 ( $4.59 \pm 0.15$ )	m
$\beta_y$	7.78	8.12 ( $7.87 \pm 0.29$ )	m
$\alpha_x$	-0.56	-0.50 ( $-0.52 \pm 0.04$ )	rad
$\alpha_y$	1.25	1.17 ( $1.16 \pm 0.09$ )	rad
Case	Measurement	Reconstruction	unit
$\epsilon_{nz}$	$137.34 \pm 17.24$	$140.05 (141.29 \pm 6.27)$	mm mrad
$\sigma_z$	$0.45 \pm 0.01$	$0.49 (0.47 \pm 0.01)$	mm
$\sigma_\delta$	$0.24 + 0.01$	$0.22 (0.22 \pm 0.00)$	%

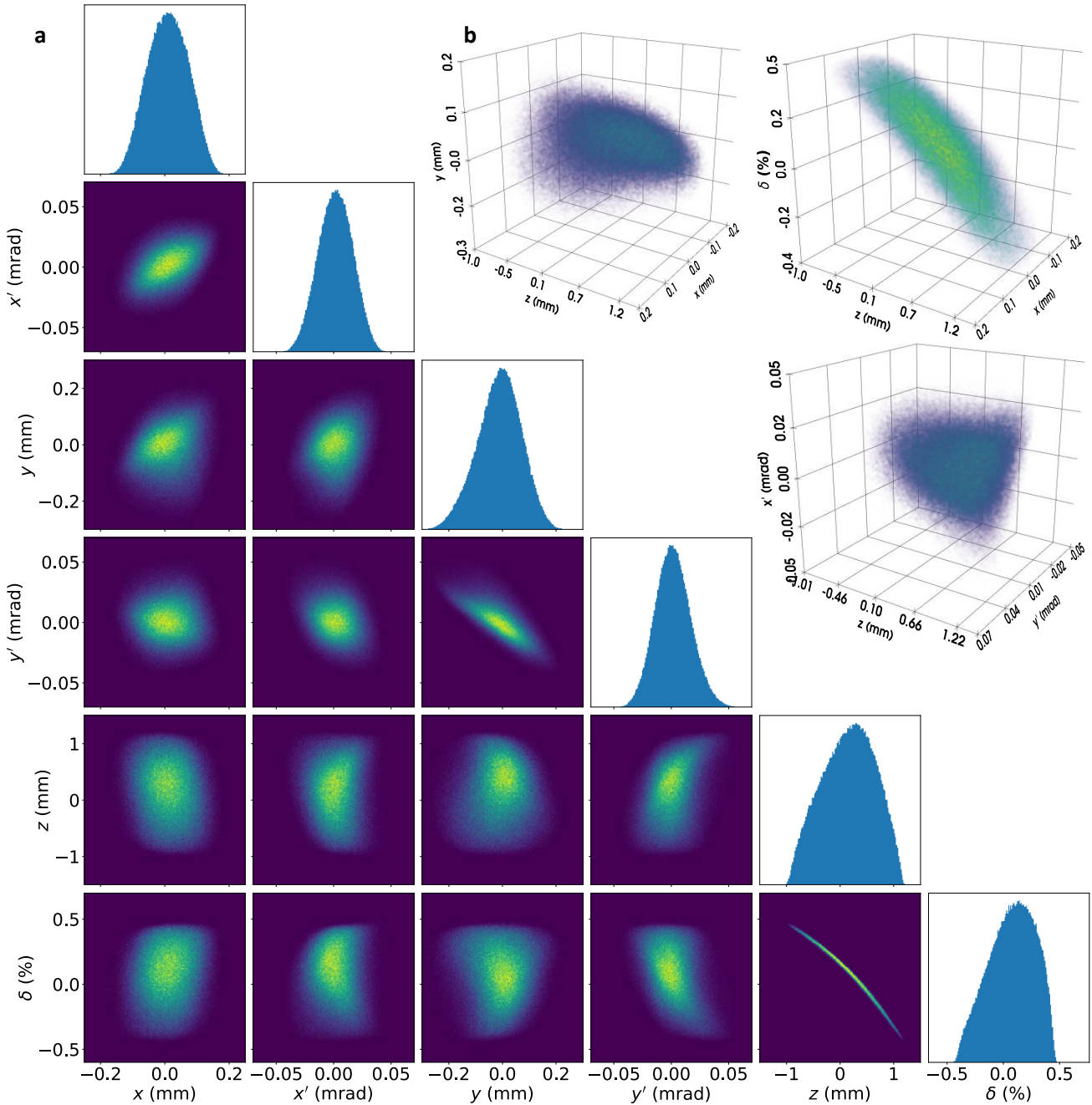


FIG. 4. **a.** Reconstructed 6-dimensional phase space. Blue histogram indicates the 1-dimensional histogram in each coordinate. **b.** 3-dimensional density plots of reconstructed beam phase spaces.

ibility and accessibility for beam diagnostics. For example, in low-energy proton and heavy-ion beam facilities, buncher cavities have been utilized with specialized bunch shape monitor (BSMs) for longitudinal emittance measurements [57–59]. It is thus expected that the reconstruction methodology, combined with systematic phase scan of the buncher cavity at the spectrometer screen and quadrupole scans, can provide not only the longitudinal phase space, but also the complete 6-dimensional phase space of the beam, without requiring the use of BSMs.

The reconstruction methodology offers broad applicability across accelerator science. In particular, the information of high-fidelity beam phase space can be used with non-differentiable simulations that consider collective and nonlinear effects. This compatibility extends its utility to a wide range of challenges in accelerator development, including beamline optimization, predictive beam characterization along multiple beamline location with forward-backward particle trackings, and model calibration for future digital twin frameworks [60, 61]. In

the context of FEL facilities, the reconstructed phase space can be applied to the measurement-based studies on suppression of emittance growth induced by the CSR effect and investigation of matching conditions along the beamline, thus to eventually enhance the FEL quality. Moreover, in advanced accelerator concepts where beam quality preservation is one of the most important tasks [62, 63], the optimization of conditions for injection into wakefields (either based on structures or plasmas) becomes critically important. The present framework provides a powerful diagnostic tool to support such optimization, thereby enhancing the performance of the future advanced acceleration schemes.

In case of the uniqueness of the beam phase space through the reconstruction process, we will perform additional dedicated investigations on uncertainty quantification to further enhance the accuracy and reliability of the reconstruction methodology.

The GPSR methodology presented in this work paves the way for significant advances in the realization of uncertainty-aware beam diagnostics with broader applicability in a variety of accelerator facilities with different particle species, including accelerator-based light sources, proton and heavy-ion accelerators, advanced accelerator concepts, and various test facilities.

### III. METHODS

#### A. PAL-XFEL

The PAL-XFEL facility consists of a photoinjector, 3 bunch compressor sections, and number of accelerator columns. The photoinjector comprises 2.856 GHz, 1.6 cell copper-cathode RF gun and two 3.0 m accelerating cavities [64, 65]. Wavelength of the UV laser illuminating the cathode is 257 nm. UV laser distribution is basically Gaussian shape in both transverse and longitudinal planes, but truncated in the transverse plane to obtain low emittance against the space charge force along the injector section. A full width at half maximum UV length was 2.8 ps. Nominal beam charge is set to 250 pC during normal operation for user service. When the beam is generated along the photoinjector, it is propagating through the laser heater and Hard X-ray Linac 1 (HL1) section as shown in Fig. 1 of Ref. [10]. The main purpose of the laser heater is to increase the slice energy spread of the beam and suppress a micro-bunching instability. The HL1 section consists of four 3.0 m accelerating cavities, with two of them interconnected as single module. Typical kinetic energy of the beam after the HL1 is approximately 380 MeV, but we turned off the second accelerating module in this demonstration to only use the XLIN as the accelerating cavity. The kinetic energy of the beam becomes reduced to 260.5 MeV.

#### B. Setup for data acquisition and GPSR training

In the demonstration section, operational phase and length of the XLIN cavity is 11.424 GHz and 0.6 m. The bending angle and arc length of the bunch compressor dipole magnet are 4.97 deg and 0.2 m, respectively. The distance between Q1 magnet and YAG1 screen is about 12.6 m. In case of the downstream validation section, the operational frequency of 1.066 m S-band TCAV is 2.856 GHz, where the spectrometer dipole magnet has the bending angle and arc length of 15 deg and 0.7 m.

We set the range of the Q1 magnet strength from  $-2.77$  to  $3.16$  T/m with 16 samples. We also set the XLIN cavity phase from  $-228.5$  to  $-193.5$  deg with 5-degree steps including XLIN turned off. The XLIN voltage used in the differentiable simulations is 8.4 MV/m, estimated by the beam energy measurement at the YAG2 screen. During the data acquisition (DAQ), the Q2 magnet was fixed at a strength of  $+2.54$  T/m while Q3 – 4 were turned off. This setting ensured that the beam size at the center of the Q1 scan range was minimized in both horizontal and vertical planes, thus forming quadratic response of the beam envelope. In addition, under these conditions, we measured the fractional energy spread distribution while minimizing the horizontal beam size contribution [66].

In the GPSR process, the initial phase space distribution was sampled from a multivariate normal distribution where the scaling factor was set to  $10^{-3}$  to ensure that the initial 6-dimensional phase space is on the order of mm in position and mrad in momentum. We used fully connected neural networks with two hidden layers connected by Tanh activation functions, where each layer contains 20 neurons. The back-propagation, based on the gradient-descent method where the learning rate was set to 0.01, was performed using a mean absolute error-based loss function estimated by the comparison between experimental measurements and predictions [44].

#### C. Beam measurements in dispersive section

During measurements in dispersive section for the reconstruction model training, a current, corresponding to the magnetic field of the BC magnets, was fixed. The change of the beam energy induced by the XLIN cavity with respect to the RF phase results in not only the evolution of the beam shape but also the shift of the beam centroid position at the YAG1 screen. Accordingly, we set the procedure for the experimental data acquisition as follows: i) we first found the phase of the XLIN that provides the minimum horizontal beam size at the YAG1 screen. This is the case where the energy chirp is minimized. ii) We then set the BC dipole current to adjust the beam position to be at the center of the YAG1 screen; this is a procedure of defining the reference case when the XLIN is turned on. At the same time, iii) we fixed the BC dipole magnetic field for data acquisition. Finally, iv) we set the XLIN phase range that provides the beam

images that are positioned within the given aspect ratio of the YAG1 screen.

#### D. Image processing and downstream measurements

When the BC is turned on, the projected beam distribution at the YAG1 screen spreads due to the energy correlation. Thus, with given amount of scintillating light, background noise becomes relatively large. To mitigate the noise, we averaged all 15 images and subtracted the background noise. The signal-to-noise ratio (SNR) value, defined as a ratio between maximum and background intensity of the image, varies depending on the beam size. The lowest observed SNR was approximately 1.6 for the case with the BC ON and XLIN OFF, which corresponds to the largest beam distribution in the dataset. Except for this case, the SNR value was generally larger than 3.0. In addition to removing the noise, we applied a Gaussian filter with the standard deviation of 2 pixels and a median filter with the kernel size of 2 to smooth the beam distribution. We also performed the threshold subtraction using the triangle threshold method [67], with the multiplication factor of 1.7. The image at the YAG1 was cropped to  $470 \times 260$  with the pixel resolution of roughly  $20.2 \mu\text{m}/\text{pixel}$  due to limited memory (40 GB) of the GPU during the GPSR training.

In case of the YAG2 screen, the calibrated energy resolution (in horizontal axis) with respect to the measured dispersion is approximately 0.004%/pixel. Likewise, the estimated TCAV calibration factors were roughly  $4.8 \mu\text{m}/\text{pixel}$  for BC OFF and  $4.4 \mu\text{m}/\text{pixel}$  for BC ON according to the TCAV voltage set to 1.7(1.1) MV for BC ON(OFF). These TCAV voltage values were used in the beam dynamics simulation with the reconstructed phase space to predict the LPS and other transverse-energy correlations which are measured downstream at the end of the beamline. During these measurements, while Q3 – 4 were turned off, Q5 – 7 were activated with the field strengths of  $-0.89$ ,  $-2.43$ , and  $5.43 \text{ T/m}$  to properly propagate the beam to the YAG2 screen.

Due to the low SNR of the YAG1 image, we suspected that some of the beam distributions were unintentionally cut off during the image processing. In contrast, the SNR of the YAG2 image was typically larger than 100. As a result, the measured LPS and  $(y, \delta)$  correlations without threshold subtraction led to underestimation of the predicted distributions. Therefore, we applied finite level of the threshold value to the YAG2 image to attenuate the beam signal and compare it with the prediction. When the BC was turned off, the threshold level of the LPS and  $(y, \delta)$  images were set to approximately  $10 - 12.5\%$  of the maximum intensity of the image. Similarly, in the case when the BC was turned on, the threshold level of the LPS image was set to roughly  $22.5\%$  of the maximum intensity. The error of the longitudinal emittance was calculated using 3 cases with different threshold levels;

$\pm 2.5\%$  based on the reference threshold value of 10%.

## IV. DATA AVAILABILITY

The data presented in this paper and other findings of this study are available from the corresponding author upon reasonable request.

## V. CODE AVAILABILITY

This research used the Bmad-X code [41] for differentiable simulations, which is available in the public repository <https://github.com/bmad-sim/Bmad-X>. The GPSR framework for the phase space reconstruction is available in the github repository <https://github.com/roussel-ryan/gpsr>.

## VI. ACKNOWLEDGEMENTS

Authors thank PAL-XFEL accelerator control team members and Prof. Moses Chung for support on the accelerator control and fruitful discussions on beam correlations in early stage of the study. This work was supported by the National Research Foundation of Korea (NRF) grant (2019R1I1A1A01041573, RS-2024-00347026, RS-2024-00455499), funded by the Korea government (MSIT). This work was also supported by the U.S. Department of Energy, Office of Science under Contract No. DE-AC02-76SF00515 and the Center for Bright Beams, NSF award PHY-1549132. This research used resources of the National Energy Research Scientific Computing Center (NERSC), a U.S. Department of Energy Office of Science User Facility located at Lawrence Berkeley National Laboratory, operated under Contract No. DE-AC02-05CH11231 using NERSC award BES-ERCAP0020725.

## VII. AUTHOR CONTRIBUTIONS

S.K. and R.R. led the conception of the GPSR methodology with standard accelerator elements. J.P.G.A. and R.R. developed the differentiable simulations and GPSR framework and Y.K.K. provided guidance and oversight. S.K. led the conceptual study including simulated demonstrations. S.K., G.K., and H.Y. performed the experiment with support from M.-H.C., C.H.S., and H.H. S.K. led the data analysis including GPSR training, tracking simulation, and data visualization. J.P.G.A., R.R., G.K., A.E., and H.Y. contributed to the data analysis and validation. S.K. and R.R. wrote the draft manuscript and S.K., R.R., and A.E. edited the manuscript. All authors reviewed and agreed to the final version of the manuscript.

## VIII. COMPETING INTERESTS

The authors declare no competing interests.

---

[1] E. A. Seddon, J. A. Clarke, D. J. Dunning, C. Masiocvecchio, C. J. Milne, F. Parmigiani, D. Rugg, J. C. H. Spence, N. R. Thompson, K. Ueda, S. M. Vinko, J. S. Wark, and W. Wurth, Short-wavelength free-electron laser sources and science: a review\*, *Reports on Progress in Physics* **80**, 115901 (2017).

[2] N. Huang, H. Deng, B. Liu, D. Wang, and Z. Zhao, Features and futures of x-ray free-electron lasers, *The Innovation* **2**, 100097 (2021).

[3] J. Andruszkow *et al.*, First observation of self-amplified spontaneous emission in a free-electron laser at 109 nm wavelength, *Phys. Rev. Lett.* **85**, 3825 (2000).

[4] M. Hogan, C. Pellegrini, J. Rosenzweig, G. Travish, A. Varfolomeev, S. Anderson, K. Bishopberger, P. Frigola, A. Murokh, N. Osmanov, S. Reiche, and A. Tremaine, Measurements of high gain and intensity fluctuations in a self-amplified, spontaneous-emission free-electron laser, *Phys. Rev. Lett.* **80**, 289 (1998).

[5] G. Geloni, E. Saldin, L. Samoylova, E. Schneidmiller, H. Sinn, T. Tschentscher, and M. Yurkov, Coherence properties of the european xfel, *New Journal of Physics* **12**, 035021 (2010).

[6] J. Amann *et al.*, Demonstration of self-seeding in a hard-x-ray free-electron laser, *Nature Photonics* **6**, 693 (2012).

[7] T. Tanaka and T. Shintake, A compact and cost-effective hard x-ray free-electron laser driven by a high-brightness and low-energy electron beam, *Nature Photonics* **6**, 540 (2012).

[8] Y. Inubushi, T. Sato, T. Tanaka, K. Tono, T. Kameshima, S. Matsuyama, Y. Furukawa, T. Togashi, S. Takahashi, H. Ohashi, *et al.*, Single shot coherence properties of the free-electron laser sacla in the hard x-ray regime, *Physical Review Letters* **109**, 144801 (2012).

[9] W. Decking, S. Abeghyan, P. Abramian, *et al.*, A mhz-repetition-rate hard x-ray free-electron laser driven by a superconducting linear accelerator, *Nature Photonics* **14**, 391 (2020).

[10] H.-S. Kang, C. Min, H. Heo, C. Kim, H.-S. Yang, S.-K. Baek, H.-S. Choi, G.-H. Mun, B.-S. Park, S.-C. Jung, G. Kim, I. Nam, S. H. Park, H. J. Suh, D. E. Shin, S.-H. Kim, S. K. Lee, B.-G. Lee, S.-Y. Lee, J. H. Lee, D.-U. Na, Y. U. Park, S. K. Park, K.-J. Kim, I. S. Ko, Y. U. Jeong, and H. J. Lee, Hard x-ray free-electron laser with femtosecond-scale timing jitter, *Nature Photonics* **11**, 708 (2017).

[11] I. Nam, C. Min, H. Heo, C. Kim, H.-S. Yang, S.-K. Baek, H.-S. Choi, G.-H. Mun, B.-S. Park, S.-C. Jung, G. Kim, H.-S. Kang, S. H. Park, H. J. Suh, D. E. Shin, S.-H. Kim, S. K. Lee, B.-G. Lee, S.-Y. Lee, J. H. Lee, D.-U. Na, Y. U. Park, S. K. Park, K.-J. Kim, I. S. Ko, Y. U. Jeong, and H. J. Lee, High-brightness self-seeded x-ray free-electron laser covering the 3.5 kev to 14.6 kev range, *Nature Photonics* **15**, 435 (2021).

[12] E. Saldin, E. Schneidmiller, and M. Yurkov, On the coherent radiation of an electron bunch moving in an arc of a circle, *Nuclear Instruments and Methods in Physics Research Section A: Accelerators, Spectrometers, Detectors and Associated Equipment* **398**, 373 (1997).

[13] S. Di Mitri and M. Cornacchia, Electron beam brightness in linac drivers for free-electron-lasers, *Physics Reports* **539**, 1 (2014).

[14] F. Zhou, K. Bane, Y. Ding, Z. Huang, H. Loos, and T. Raubenheimer, Measurements and analysis of a high-brightness electron beam collimated in a magnetic bunch compressor, *Phys. Rev. ST Accel. Beams* **18**, 050702 (2015).

[15] Y. Ding, K. L. F. Bane, W. Colocho, F.-J. Decker, P. Emma, J. Frisch, M. W. Guetg, Z. Huang, R. Iverson, J. Krzywinski, H. Loos, A. Lutman, T. J. Maxwell, H.-D. Nuhn, D. Ratner, J. Turner, J. Welch, and F. Zhou, Beam shaping to improve the free-electron laser performance at the linac coherent light source, *Phys. Rev. Accel. Beams* **19**, 100703 (2016).

[16] J. Qiang, Y. Ding, P. Emma, Z. Huang, D. Ratner, T. O. Raubenheimer, M. Venturini, and F. Zhou, Start-to-end simulation of the shot-noise driven microbunching instability experiment at the linac coherent light source, *Phys. Rev. Accel. Beams* **20**, 054402 (2017).

[17] D. Ratner, C. Behrens, Y. Ding, Z. Huang, A. Marinelli, T. Maxwell, and F. Zhou, Time-resolved imaging of the microbunching instability and energy spread at the linac coherent light source, *Phys. Rev. ST Accel. Beams* **18**, 030704 (2015).

[18] M. Zhang, *Emittance formula for slits and pepper-pot measurement*, Tech. Rep. FNAL-TM-1988 (Fermi National Accelerator Laboratory, 1996).

[19] P. Lu, H. Vennekate, A. Arnold, P. Michel, P. Murcek, J. Teichert, and R. Xiang, Transverse emittance measurement by slit-scan method for an srf photo injector, in *Proceedings of the 35th International Free Electron Laser Conference (FEL 2013)* (2013) pp. 322–325.

[20] C. McKee, P. O’Shea, and J. Maday, Phase space tomography of relativistic electron beams, *Nuclear Instruments and Methods in Physics Research Section A: Accelerators, Spectrometers, Detectors and Associated Equipment* **358**, 264 (1995).

[21] V. Yakimenko, M. Babzien, I. Ben-Zvi, R. Malone, and X.-J. Wang, Electron beam phase-space measurement using a high-precision tomography technique, *Phys. Rev. ST Accel. Beams* **6**, 122801 (2003).

[22] D. Xiang, Y.-C. Du, L.-X. Yan, R.-K. Li, W.-H. Huang, C.-X. Tang, and Y.-Z. Lin, Transverse phase space tomography using a solenoid applied to a thermal emittance measurement, *Phys. Rev. ST Accel. Beams* **12**, 022801 (2009).

[23] K. Hock and A. Wolski, Tomographic reconstruction of the full 4d transverse phase space, *Nuclear Instruments and Methods in Physics Research Section A: Accelerators, Spectrometers, Detectors and Associated Equipment* **726**, 8 (2013).

[24] B. Hermann, V. A. Guzenko, O. R. Hürzeler, A. Kirchner, G. L. Orlandi, E. Prat, and R. Ischebeck, Electron beam transverse phase space tomography using nanofabricated wire scanners with submicrometer resolution, *Phys. Rev. Accel. Beams* **24**, 022802 (2021).

[25] A. Hoover, K. Ruisard, A. Aleksandrov, A. Zhukov, and S. Cousineau, Analysis of a hadron beam in five-dimensional phase space, *Phys. Rev. Accel. Beams* **26**, 064202 (2023).

[26] S. Jaster-Merz, R. W. Assmann, R. Brinkmann, F. Burkart, W. Hillert, M. Stanitzki, and T. Vinatier, 5d tomographic phase-space reconstruction of particle bunches, *Phys. Rev. Accel. Beams* **27**, 072801 (2024).

[27] B. Cathey, S. Cousineau, A. Aleksandrov, and A. Zhukov, First six dimensional phase space measurement of an accelerator beam, *Phys. Rev. Lett.* **121**, 064804 (2018).

[28] P. Emma, J. Frisch, and P. Krejcik, A transverse rf deflecting structure for bunch length and phase space diagnostics, LCLS Technical Note **12** (2000).

[29] P. J. Emma, *Bunch Length Measurements Using a Transverse RF Deflecting Structure in the SLAC Linac*, Tech. Rep. SLAC-PUB-9241 (SLAC National Accelerator Laboratory, 2002).

[30] Y. Ding, C. Behrens, P. Emma, J. Frisch, Z. Huang, H. Loos, P. Krejcik, and M.-H. Wang, Femtosecond x-ray pulse temporal characterization in free-electron lasers using a transverse deflector, *Phys. Rev. ST Accel. Beams* **14**, 120701 (2011).

[31] B. Marchetti, A. Grudiev, and W. Wuensch, Experimental demonstration of novel beam characterization using a polarizable x-band transverse deflection structure, *Scientific Reports* **11**, 3560 (2021).

[32] A. L. Edelen, S. G. Biedron, B. E. Chase, D. Edstrom, S. V. Milton, and P. Stabile, Neural networks for modeling and control of particle accelerators, *IEEE Transactions on Nuclear Science* **63**, 878 (2016).

[33] A. Edelen, C. Mayes, D. Bowring, D. Ratner, A. Adelmann, R. Ischebeck, J. Snuverink, I. Agapov, R. Kammering, J. Edelen, I. Bazarov, G. Valentino, and J. Wenninger, *Opportunities in machine learning for particle accelerators* (2018), arXiv:1811.03172 [physics.acc-ph].

[34] C. Emma, A. Edelen, M. J. Hogan, B. O'Shea, G. White, and V. Yakimenko, Machine learning-based longitudinal phase space prediction of particle accelerators, *Phys. Rev. Accel. Beams* **21**, 112802 (2018).

[35] A. Edelen, N. Neveu, M. Frey, Y. Huber, C. Mayes, and A. Adelmann, Machine learning for orders of magnitude speedup in multiobjective optimization of particle accelerator systems, *Phys. Rev. Accel. Beams* **23**, 044601 (2020).

[36] A. Scheinker, A. Edelen, D. Bohler, C. Emma, and A. Lutman, Demonstration of model-independent control of the longitudinal phase space of electron beams in the linac-coherent light source with femtosecond resolution, *Phys. Rev. Lett.* **121**, 044801 (2018).

[37] A. Scheinker, D. Bohler, S. Tomin, R. Kammering, I. Zagorodnov, H. Schlarb, M. Scholz, B. Beutner, and W. Decking, Model-independent tuning for maximizing free electron laser pulse energy, *Phys. Rev. Accel. Beams* **22**, 082802 (2019).

[38] A. Scheinker, F. Cropp, S. Paiagua, and D. Filippetto, An adaptive approach to machine learning for compact particle accelerators, *Scientific Reports* **11**, 19187 (2021).

[39] A. Scheinker, cDVAE: VAE-guided diffusion for particle accelerator beam 6D phase space projection diagnostics, *Scientific Reports* **14**, 29303 (2024).

[40] R. Roussel, A. Edelen, C. Mayes, D. Ratner, J. P. Gonzalez-Aguilera, S. Kim, E. Wisniewski, and J. Power, Phase space reconstruction from accelerator beam measurements using neural networks and differentiable simulations, *Phys. Rev. Lett.* **130**, 145001 (2023).

[41] J. Gonzalez-Aguilera, Y.-K. Kim, R. Roussel, A. Edelen, and C. Mayes, Towards fully differentiable accelerator modeling, in *Proc. IPAC'23* (2023) pp. 2797–2800.

[42] D. P. Kingma and J. Ba, *Adam: A method for stochastic optimization* (2017), arXiv:1412.6980 [cs.LG].

[43] S. Kim, J. P. Gonzalez-Aguilera, P. Piot, G. Chen, S. Doran, Y.-K. Kim, W. Liu, C. Whiteford, E. Wisniewski, A. Edelen, R. Roussel, and J. Power, Four-dimensional phase-space reconstruction of flat and magnetized beams using neural networks and differentiable simulations, *Phys. Rev. Accel. Beams* **27**, 074601 (2024).

[44] R. Roussel, J. P. Gonzalez-Aguilera, E. Wisniewski, A. Ody, W. Liu, J. Power, Y.-K. Kim, and A. Edelen, Efficient six-dimensional phase space reconstructions from experimental measurements using generative machine learning, *Phys. Rev. Accel. Beams* **27**, 094601 (2024).

[45] M. E. Conde, J. G. Power, W. Gai, W. Liu, P. Schoessow, X. Sun, C. Wang, E. Wisniewski, and D. Doran, Research program and recent results at the argonne wakefield accelerator facility (AWA), in *Proceedings of the Particle Accelerator Conference (PAC'05)*, JaCoW (IEEE, Knoxville, Tennessee, USA, 2005) pp. 4289–4291.

[46] V. Yakimenko, L. Alsberg, E. Bong, G. Bouchard, C. Clarke, C. Emma, S. Green, C. Hast, M. J. Hogan, J. Seabury, N. Lipkowitz, B. O'Shea, D. Storey, G. White, and G. Yocky, Facet-ii facility for advanced accelerator experimental tests, *Phys. Rev. Accel. Beams* **22**, 101301 (2019).

[47] I. S. Ko *et al.*, Construction and commissioning of pal-xfel facility, *Applied Sciences* **7**, 10.3390/app7050479 (2017).

[48] D. Dowell, P. Bolton, J. Clendenin, S. Gierman, C. Limborg, B. Murphy, and J. Schmerge, Analysis of slice emittance measurements for the slac gun test facility, in *Proceedings of the 2003 Particle Accelerator Conference*, Vol. 3 (2003) pp. 2104–2106 vol.3.

[49] D. Dowell, P. Bolton, J. Clendenin, S. Gierman, C. Limborg, B. Murphy, J. Schmerge, and T. Shaftan, Longitudinal emittance measurements at the slac gun test facility, *Nuclear Instruments and Methods in Physics Research Section A: Accelerators, Spectrometers, Detectors and Associated Equipment* **507**, 331 (2003), proceedings of the 24th International Free Electron Laser Conference and the 9th Users Workshop.

[50] K. Floettmann, Some basic features of the beam emittance, *Phys. Rev. ST Accel. Beams* **6**, 034202 (2003).

[51] B. H. Schaap and P. Musumeci, Tomography of longitudinal phase space linearization for the generation of attosecond electron bunches, *Phys. Rev. Accel. Beams* **28**, 012802 (2025).

[52] P. Emma, *X-Band RF Harmonic Compensation for Linear Bunch Compression in the LCLS*, Tech. Rep. SLAC-TN-05-004 (SLAC National Accelerator Laboratory, 2005).

[53] H.-G. Lee and et al., Technical overview of bunch compressor system for pal xfel, in *Proc. IPAC'15*, 6 (JaCoW

Publishing, Geneva, Switzerland, 2015) pp. 3018–3020.

[54] A. Paszke, S. Gross, F. Massa, A. Lerer, J. Bradbury, G. Chanan, T. Killeen, Z. Lin, N. Gimelshein, L. Antiga, A. Desmaison, A. Kopf, E. Yang, Z. DeVito, M. Raison, A. Tejani, S. Chilamkurthy, B. Steiner, L. Fang, J. Bai, and S. Chintala, Pytorch: An imperative style, high-performance deep learning library, in *Advances in Neural Information Processing Systems*, Vol. 32, edited by H. Wallach, H. Larochelle, A. Beygelzimer, F. d'Alché-Buc, E. Fox, and R. Garnett (Curran Associates, Inc., 2019).

[55] M. Borland *et al.*, A flexible sdds-compliant code for accelerator simulation, Proceedings of the 1995 Particle Accelerator Conference , 2137 (1995).

[56] NERSC, [Perlmutter](#) (2022), accessed: 2025-05-9.

[57] G. Bellodi and et al., Longitudinal beam profile measurements in linac4 commissioning, in *Proc. LINAC2014*, 0 (JACoW Publishing, Geneva, Switzerland, 2014) pp. 108–110.

[58] S. Lauber, K. Aulenbacher, W. Barth, F. Dziuba, J. List, C. Burandt, V. Gettmann, T. Kürzeder, M. Miski-Oglu, P. Forck, M. Heilmann, A. Rubin, T. Sieber, S. Yaramyshev, H. Podlech, and M. Schwarz, Longitudinal phase space reconstruction for a heavy ion accelerator, *Phys. Rev. Accel. Beams* **23**, 114201 (2020).

[59] R. Kitamura, K. Futatsukawa, N. Hayashi, K. Hirano, Y. Kondo, S. Kosaka, T. Miyao, T. Morishita, Y. Nemoto, and H. Oguri, Measurement of the longitudinal bunch-shape distribution for a high-intensity negative hydrogen ion beam in the low-energy region, *Phys. Rev. Accel. Beams* **26**, 032802 (2023).

[60] A. Edelen *et al.*, Progress on combining digital twins and machine learning-based control for accelerators at SLAC, *JACoW IPAC2024*, TUPS72 (2024).

[61] A. Edelen *et al.*, *Digital Twins for Enhanced Modeling and Control of Light Sources and Neutron Sources*, Tech. Rep. SLAC-DTRD-RFI-2024 (SLAC National Accelerator Laboratory, 2024) submitted in response to the Networking and Information Technology Research and Development (NITRD) Request for Information on Digital Twins Research and Development (Federal Register 89 FR 51554).

[62] C. A. Lindstrøm, J. M. Garland, S. Schröder, L. Boulton, G. Boyle, J. Chappell, R. D'Arcy, P. Gonzalez, A. Knetsch, V. Libov, G. Loisch, A. Martinez de la Ossa, P. Niknejadi, K. Pöder, L. Schaper, B. Schmidt, B. Sheeran, S. Wesch, J. Wood, and J. Osterhoff, Energy-spread preservation and high efficiency in a plasma-wakefield accelerator, *Phys. Rev. Lett.* **126**, 014801 (2021).

[63] C. A. Lindstrøm, J. Beinortaité, J. B. Svensson, L. Boulton, J. Chappell, S. Diederichs, B. Foster, J. M. Garland, P. G. Caminal, G. Loisch, F. Peña, S. Schröder, M. Thévenet, S. Wesch, M. Wing, J. C. Wood, R. D'Arcy, and J. Osterhoff, Emittance preservation in a plasma-wakefield accelerator, *Nature Communications* **15**, 6097 (2024).

[64] J. H. Hong, M. Chae, J. Han, H.-S. Kang, C.-K. Min, S. Park, Y. Park, and I. Ko, Beam measurement of photocathode rf-gun for pal-xfel, in *Proc. FEL2014* (2014) pp. 699–702.

[65] J. Hong, J.-H. Han, S. Park, Y. Jung, D. Kim, H.-S. Kang, and J. Pfleuger, A study on low emittance injector and undulator for pal-xfel, *High Power Laser Science and Engineering* **3**, e21 (2015).

[66] Q. Gao, J. Shi, H. Chen, G. Ha, J. G. Power, M. Conde, and W. Gai, Single-shot wakefield measurement system, *Phys. Rev. Accel. Beams* **21**, 062801 (2018).

[67] G. W. Zack, W. E. Rogers, and S. A. Latt, Automatic measurement of sister chromatid exchange frequency., *Journal of Histochemistry & Cytochemistry* **25**, 741 (1977), PMID: 70454, <https://doi.org/10.1177/25.7.70454>.